 doi:10.20944/preprints202207.0011.v1

Article

Optimization Methodology of the Magnetic Navigation System with Gradient and Uniform Saddle Coils

Sungjun Kim, Mingyu Cho, Seyeong Im, Joongho Yun, and Jaekwang Nam *

Department of Robotics, Kwangwoon University, Seoul 01897, Korea;
kxt1234@naver.com (S.K.); alsrb77022@naver.com (M.C.); syl1219ss@naver.com (S.I.); tygh7892@naver.com (J.Y.)
* Correspondence: jk2020@kw.ac.kr

Abstract: The magnetic navigation system (MNS) with gradient and uniform saddle coils is one of the effective systems to manipulate various medical magnetic robot due to its compact structure and uniformity of the magnetic field and field gradient. However, it has limited operating time and large inductance effect due to the high current density and numerous turns of coils, respectively. In this paper, we propose an optimization methodology of the MNS considering the current density and inductance of the coils. We introduce objective functions, constraints, and design variables of the MNS. Then, the MNS was designed by an optimization algorithm. The constructed MNS was compared with the conventional MNS, and it could generate 22 % stronger magnetic field or field gradient while the maximum three-dimensional rotating magnetic field was improved by 42 %. We also demonstrated an unclogging performance of a helical robot was improved by 54 % with the constructed MNS.

Keywords: magnetic navigation system; saddle coil; optimization; magnetic robot; magnetic field

1. Introduction

Various magnetic robots and tools have attracted a great deal of attention as an alternative to conventional medical devices such as catheter, endoscope, gripper and forceps [1–7]. Remote magnetic actuation not only provides an unlimited operation time but also gives an advantage of being able to miniaturize the robot because it needs no batteries. These advantages make magnetic robots suitable for minimally invasive medical devices that must operate for a long time inside small and narrow human organs. However, the magnetic robots require a magnetic navigation system (MNS) that generates an external magnetic field outside the magnetic robots.

One simple combination for the MNS is combing several pairs of Helmholtz coils (HCs) and Maxwell coils (MCs). Theses circular coils are structurally simple and need no localization by providing the same magnetic field or field gradient over the large workspace. Thus, many researchers have utilized these combinations to actuate the magnetic robots [8–15]. Three pairs of HCs is a basic combination to generate a three-dimensional (3D) magnetic field [8–10]. Several pairs of MCs also can be integrated with the HCs to generate both the magnetic field and the field gradient [11–13]. However, combining multiple circular pairs of coils are geometrical inefficient. These combinations produce large empty spaces between the pairs of coils. To solve this problem, the rotatable MNSs have been developed [14,15]. Instead of increasing the number of coils, the position of the coils can be controlled to secure the required degree of freedom (DOF). However, this method makes the MNS complex because it requires additional electro-mechanical systems. As another solution, uniform saddle coil (USC) and gradient saddle coil (GSC) have been developed [16]. These coils can surround the circular coils to forms compact cylindrical structure without extra spaces. Also, cylindrical shape is appropriate to ac-

 doi:10.20944/preprints202207.0011.v1

commodate the human body as well as other similar medical devices such as the magnetic resonance imaging (MRI) machine and computerized tomography (CT) scanners. There are various combinations of the circular and saddle coils [16–20]. Especially, the MNS composed of five pair of coils (two USCs, a GSC, a HC, and a MC) can generate a 3D rotation and two-dimensional (2D) translation of the magnetic robots [17]. However, the conventional MNS with five pair of coils was not optimized through electromagnetic design process. Thus, the coils cannot utilize the maximum output power of the power supply unit due to either too large or too small coil resistance. An inductance effect that attenuates a time-varying magnetic field also was not considered. Heat generation due to the current can be another design factor because it can reduce the magnetic field and the operating time limit.

In this paper, an electromagnetic optimization methodology is proposed for the MNS having the five pair of coils. First, two pipes to install the five pairs of coils are determined to have required inner space. Then, we propose a novel arrangement of five pairs of coils which enable the MNS to generate similar three-axis magnetic fields per current, because the available amplitude of a 3D rotating magnetic field is restricted by the coil that generates the smallest magnetic field. Next, the design variables and constraints are defined for the optimization with some assumptions to simplify the calculation. The constraints include the inductance effect and heat generation of the coils so that the MNS can generate strong time-varying magnetic field under given temperature limit. The MNS is designed an optimization algorithm with the given constraints. We first measured the performance of the optimized MNS. Then, we compared the optimized MNS with the conventional MNS. We also demonstrated that the optimized MNS could effectively improve the performance of a magnetic robot.

2. Electromagnetic optimization of the MNS

2.1. Magnetic field and field gradient generated by each pair of coils

The magnetic field and the field gradient from the MNS produce a magnetic torque and a force for a magnetic robot to generate a rotation and a translation motion [18]. This torque and force can be expressed as:

$$\vec{F} = (\vec{m} \cdot \nabla)\vec{B} \tag{1}$$

$$\vec{T} = (\vec{m} \times \vec{B}) \tag{2}$$

where $\vec{m}$ is a magnetic moment of the robot and $\vec{B}$ is the external magnetic field. This external magnetic field can be generated by the five pairs of coils as shown in Figure 1, and three components of the magnetic field vector can be expressed as [16]:

$$\vec{B}_{MNS} = \begin{bmatrix} B_h + (G_g + G_m)x \\ B_{uy} + (-2.4398G_g - 0.5G_m)y \\ B_{uz} + (1.4398G_g - 0.5G_m)z \end{bmatrix} \tag{3}$$

$$B_h = (4/5)^{3/2} N_h I_h \mu_0 / r_h,\ B_{uy} = 0.6004 N_{uy} I_{uy} \mu_0 / r_{uy},\ B_{uz} = 0.6004 N_{uz} I_{uz} \mu_0 / r_{uz},$$
$$G_m = (16/3)(3/7)^{5/2} N_m I_m \mu_0 / r_m^2,\ G_g = 0.3286 N_g I_g \mu_0 / r_g^2$$

where N_k, I_k, and r_k are the number of turns, current, and radius of the kth coil, and the subscripts h, m, g, uy, and uz represent the HC, MC, GSC, y- and z-directional USCs, respectively. Also, μ_0 is the magnetic permeability of free space. In Equation (3), x, y, and z are assumed to be negligible around the center of the MNS where the workspace is. Then, the magnetic torque is generated by the three components (B_h, B_{uy}, and B_{uz}) while the magnetic force is generated by the two components (G_g and G_m).

Preprints (www.preprints.org) | NOT PEER-REVIEWED | Posted: 1 July 2022 doi:10.20944/preprints202207.0011.v1

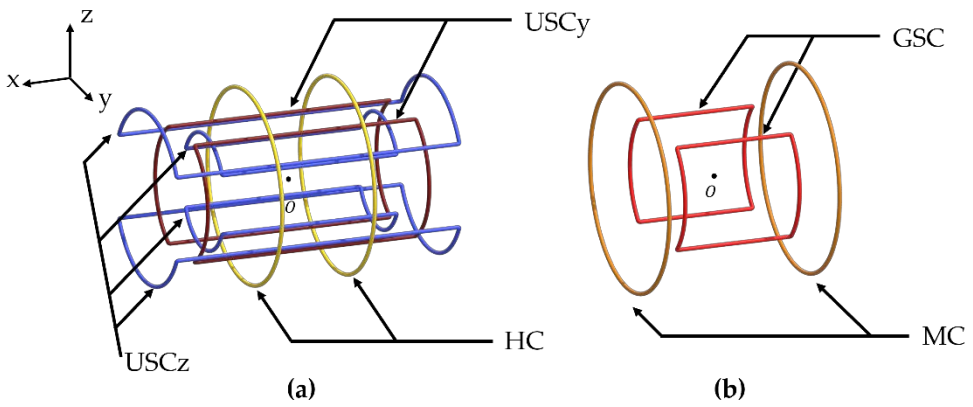

Figure 1. The novel arrangement of five pairs of coils which enable the MNS to generate the maximum 3D rotating magnetic field. (a) The three pairs of coils (HC, USCy, and USCz) for the uniform magnetic field. Here, the USCz is divided into the USCz1 and USCz2. (b) The two pairs of coils (MC and GSC) for the uniform magnetic field gradient.

2.2. Frame of the MNS

Pipes are used for the frame of the MNS due to its cylinderical structure. Figure 2(a) shows the configuration of the MNS using the two pipes. Since the coils can be attatched to both side of the pipes, the two pipes are enough to install all coils. Considering the volume and the magnetic field of the MNS, we determine the diameter of each pipe. If the diameter is too small, the MNS cannot have enough inner space for the magnetic robots. In contrast, if the diameter is too large, the coils cannot generate strong enough magnetic field to actuate the magnetic robots. Based on these idea, the inner and outer diameters of the pipes (d_{in} and d_{out}) are determined by 31 cm and 46 cm, respectively. The thickness of the pipes (t_p) is equal to 5 mm, and the gap between the pipes (d_{gap}) is 7 cm. The pipes have four squre windows to observe the inner space of the MNS during experiments.

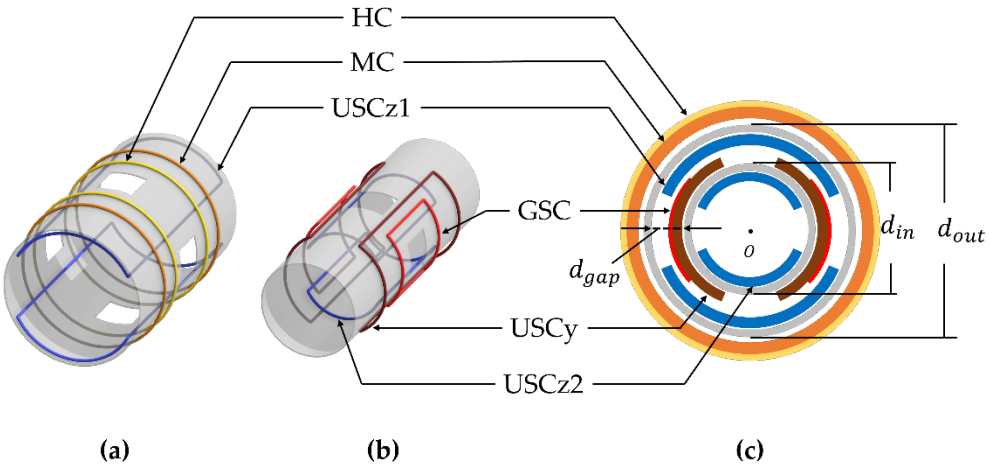

Figure 2. (a) The HC and MC are installed outside the outer pipe, and the USCz1 is installed inside the outer pipe. (b) The USCy and GSC are installed outside the inner pipe, and the USCz2 is installed inside the inner pipe. (c) The five pairs of coils integrated with the two pipes.

2.3. Arrangement of the MNS

Various mechanisms of the magnetic robots are based on the 3D rotating magnetic field, and the available amplitude of the 3D rotating magnetic field is restricted by the coil that generates the smallest magnetic field. Thus, it is preferable that the three components of magnetic field (B_h, B_{uy}, and B_{uz}) have the same value. In Equation (3), the HC

Preprints (www.preprints.org) | NOT PEER-REVIEWED | Posted: 1 July 2022 doi:10.20944/preprints202207.0011.v1

can generate a larger magnetic field than the USC with the same conditions (N_k, I_k, and r_k). Thus, the HC should be placed outside the USC. Then, B_h can be equal to B_{uy} or B_{uz} with the larger radius. However, since USCy and USCz are the same type of the coil, if the same N_k and I_k are given, the magnetic field generated by the outer coil is inevitably small. To solve this problem, we divide the USCz and place the USCy between them while the USCz1 and USCz2 are connected in series. Then, the USCy and USCz can generate the same magnetic field (B_{uy} and B_{uz}) by adjusting the ratio of the USCz1 and USCz2.

Figure 2 shows this novel arrangement with the divided USCz. If we use two pipes, this arrangement is the only possible case. We then place the MC and GSC in the empty spaces. The MC is placed on the outermost side of the MNS because it can be overlapped with the HC. In contrast, the GSC can be overlapped with the USCy and USCz. Especially, the GSC can generate the strongest magnetic field gradient if it is place with the USCz, but in this case the GSC reduce the inner space of the MNS because the GSC is thicker than the divided coil (USCz2). Thus, we place the GSC with the USCy.

2.4. Objective function and design variables of each coil

The MNS has three components of the magnetic field (B_h, B_{uy}, and B_{uz}) and two components of the field gradient (G_g and G_m). We assume that the maximum output of a power supply unit (P_{out}) is utilized for each coil. Then, the five components of MNS can be rewritten as

$$B_{k,max} = \frac{n_k N_k \mu_0}{r_k} \sqrt{\frac{P_{out}}{R_k}} \tag{4}$$

$$G_{k,max} = \frac{n_k N_k \mu_0}{r_k^2} \sqrt{\frac{P_{out}}{R_k}} \tag{5}$$

where n_k and R_k are the coefficient of the kth coil in Equation (3) and the resistance of the kth coil. These five components become the objective functions of each coil, and our goal is maximizing these values with several constraints in Section 2.5. In this paper, we define the design variables as the number of turns (N_k) and thickness of wire (t_k) of the coils. Then, we can reorganize the objective functions using design variables. In the Equations (4)-(5), the resistance (R_k) of the kth coil can be expressed as

$$R_k = \frac{l_k}{A_k} \rho_{coil} \tag{6}$$

where l_k, A_k and ρ_k are the total length, cross-sectional area, and resistivity of the wire wound N_k turns. In Equation (6), the cross-sectional area (A_k) can be calculated assuming a circular wire, and the total length (l_k) is calculated assuming that the wire is only wound at the center of the coil. As a result, l_k and A_k are calculated as follows:

$$l_k = c_k r_k N_k \tag{7}$$

$$c_{h,m} = 4\pi,\ c_{uy,uz} = 22.3788,\ c_g = 13.3704$$

$$A_k = \pi t_k^2 / 4 \tag{8}$$

where c_k is the geometrical coefficient of the kth coil. In Equation (7), r_k can be calculated assuming that the bundle of wire forms a square cross section as shown in Figure 3. Although the actual cross section is close to a circle, this assumption is valid because the ra-

Preprints (www.preprints.org) | NOT PEER-REVIEWED | Posted: 1 July 2022 doi:10.20944/preprints202207.0011.v1

dius of the bundle is very small compared to the radius of the coil. Then, r_k can be expressed as

$$r_k = 0.5d_k \pm 0.5t_k\sqrt{N_k}$$
$$d_{h,m} = d_{out},\ d_{uz1} = d_{out} - 2t_p,\ d_{uy,g} = d_{in},\ d_{uz2} = d_{in} - 2t_p \quad (9)$$

where d_k is the outer or inner diameter of the pipe to which the kth coil is attached. In Equation (9), the sign is determined depending on where the coil is attached to the pipe. If the coil is attached to the outside, it has the plus sign (+), and if the coil is attached to the inside, it has the minus sign (-). Finally, the objective functions can be rewritten using two design variables (N_k and t_k) by substituting Equations (6)-(9) into Equations (4)-(5):

$$B_{k,\max} = \frac{\mu_0 n_k t_k}{\left(0.5d_k \pm 0.5t_k\sqrt{N_k}\right)^{3/2}}\sqrt{\frac{\pi N_k P_{out}}{4c_k\rho_{coil}}} \quad (10)$$

$$G_{k,\max} = \frac{\mu_0 n_k t_k}{\left(0.5d_k \pm 0.5t_k\sqrt{N_k}\right)^{5/2}}\sqrt{\frac{\pi N_k P_{out}}{4c_k\rho_{coil}}} \quad (11)$$

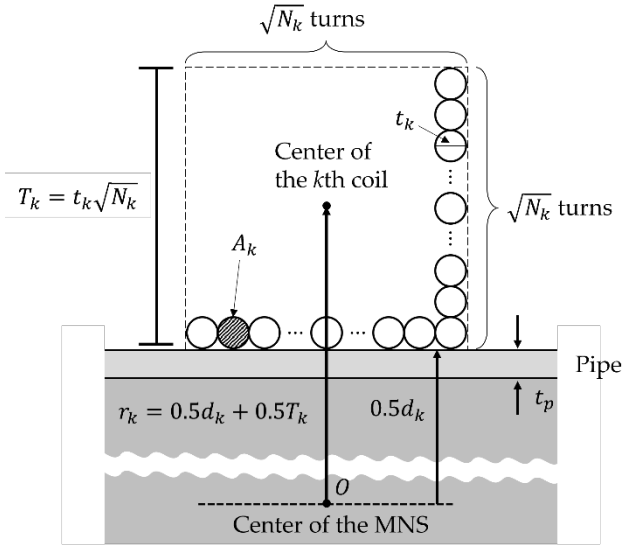

Figure 3. The design variables and parameters of the kth coil. This cross section shows the case that the coil is attached outside the pipe.

2.5. Electromagnetic and geometric constraints

We consider several electromagnetic and geometric constraints to optimize the MNS. The first constraint is that the three components of the magnetic field using the maximum power is equal:

$$B_{h,max} = B_{uy,max} = B_{uz,max} \quad (12)$$

This constraint is already described in Section 2.3. Using this constraint, we can maximize the 3D rotating magnetic field. We also consider the temperature rise of the coils because an insulated wire has an allowable temperature for safe use, and this temperature limits the available operating time of each coil. Furthermore, the temperature rise deteriorates the performance of the MNS due to the increment of the resistivity. Since the temperature of a coil is proportional to the current density, the larger cross-sectional ar-

Preprints (www.preprints.org) | NOT PEER-REVIEWED | Posted: 1 July 2022 doi:10.20944/preprints202207.0011.v1

ea of a coil makes the longer operating time limit. However, the USCy, USCz1 and GSC share the limited gap space between the pipes as shown in Figure 2(c). To enlarge the cross-sectional area without interference of the coils, we introduce constraints as follows:

$$T_{uy} + T_{uz1} < d_{gap} \tag{13}$$

$$T_g + T_{uz1} < d_{gap} \tag{14}$$

$$0.5d_{gap} < T_k \tag{15}$$

In Equation (15), T_{uz1} and T_{uz2} are not considered, but their summation ($T_{uz1} + T_{uz2}$) is considered as integrated T_{uz}. We then consider the inductance of the coils (L_k). The inductance attenuates a time-varying current of a coil. Thus, the small inductance is advantageous to generate a strong time-varying magnetic field. Because the inductance is proportional to N_k, we can obtain small inductance by reducing N_k in the given T_k. However, it reduces R_k in Equation (6) by increasing A_k and decreasing l_k. Figure 4 shows the output range of the power supply unit (3001iX by California Instruments), and the resistance must be in the range of 8.62 Ω ≤ R_k ≤ 19.05 Ω to utilize maximum power. Thus, the resistance of each coil is constrained as the minimum value:

$$R_k = 8.62\ \Omega \tag{16}$$

We also constrain t_k because too thick wire is hard to be wound. We experientially introduce a constraint as

$$t_k < 2\ \text{mm} \tag{17}$$

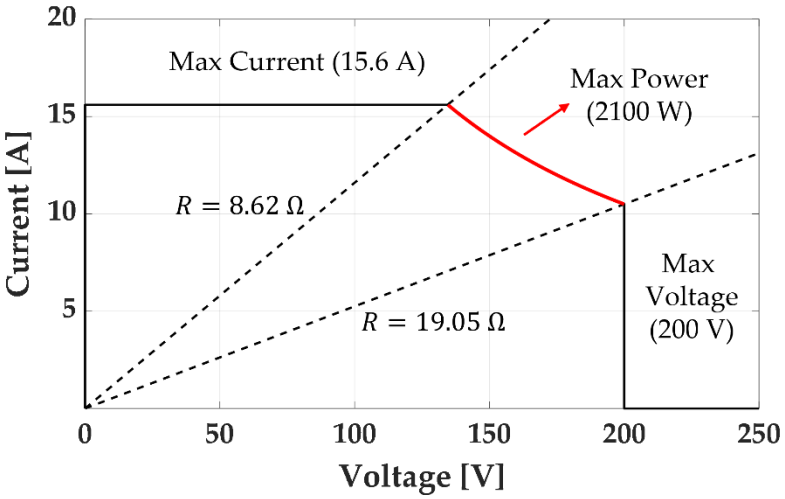

Figure 4. The output range of the power supply unit (3001iX by California Instruments).

2.6. Algorithm to optimize the MNS

We develop an optimization algorithm using Equation (10)-(11) and the given constraints. Figure 5 shows the developed algorithm. For the algorithm, we set the range of two variables as 0.001 ≤ t_k ≤ 2 and 1 ≤ N_k < 1420. The range of t_k is determined by Equation (17) and the minimum incremental value of 0.001 mm. The maximum turns of coils between the pipes are 1420 in the case that t_k has the minimum value of 0.001 mm. Thus, the maximum limit of N_k become 1420. Using this algorithm, we obtain optimized MNS and its result is shown in Table 1.

Preprints (www.preprints.org) | NOT PEER-REVIEWED | Posted: 1 July 2022 doi:10.20944/preprints202207.0011.v1

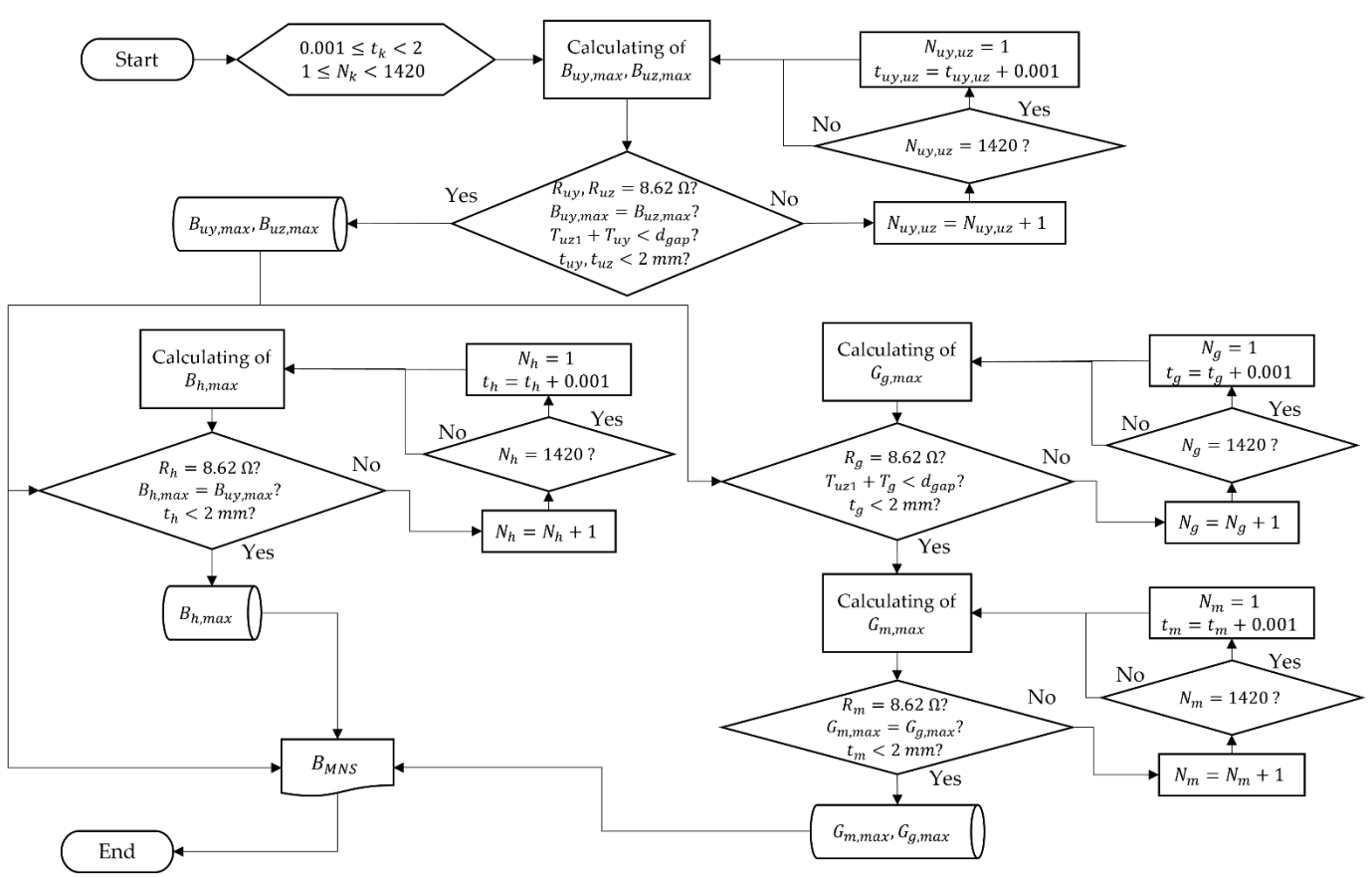

Figure 5. Algorithm to optimize the MNS with the given constraints.

Table 1. Designed major variables of the MNS.

Variables	HC	USCy	USCz1	USCz2	MC	GSC
Radius of the coil (r_k) [mm]	249.8	173.1	220.0	137.0	248.2	173.2
Resistance of the coil (R_k) [Ω]	8.62	8.62	8.64		8.62	8.63
Thickness of the wire (t_k) [mm]	1.86	1.89	1.59		1.79	1.65
Turns of the wire (N_k) [turns]	448	370	40	269	413	479
Max magnetic field ($B_{k,max}$) [mT] or field gradient ($G_{k,max}$) [mT/m]	25.16	25.15	25.26		84.26	102.99

3. Environment and verification

3.1. Construction and verification of the MNS

3.1.1 Construction of the MNS

The optimized MNS was constructed as shown in Figure 6, and major variables were measured as shown in Table 2. In the figure, each coil was connected to the power supply unit (3001iX by Califonia Instruments). A magnetic robot inside the MNS is tracked by a real-time camera and controlled by the joystic controller. The two pipes for the coils were made of fiber-reinforced plastic that can withstand the weight and heat of the coils. The plastic is nonmetalic material, so the pipes have no iron loss that attenuates the magnetic field. In contrast, the structure to support the pipes was made of metalic aluminium. Although aluminium can have iron loss, the iron loss cannot affect the magnetic field inside the MNS because the structure is located outside the coils.

The constructed MNS has considerable geometrical errors because each coil could not be precisely manufactured. There is no available winding machine for the coils due

Preprints (www.preprints.org) | NOT PEER-REVIEWED | Posted: 1 July 2022 doi:10.20944/preprints202207.0011.v1

to their unusual size and shape. In particular, since the circular HC and MC are attached to the outside of the circular pipe, if the radius (r_k) is smaller than the designed value, it cannot be assembled with the pipe. Thus, margin was added to manurfacture the HC and MC while the other saddle coils were manufactured without margin. As a result, $B_{k,max}$ and $G_{k,max}$ of the HC and MC were measured to be significantly smaller than the design values as shown in Table 2. This error can be reflected by correction factors which are the ratio of the measured and designed values. Table 3 shows the correction factors, and the correct B_k or G_k can be obtained by multiplying the correction factor and the each designed B_k or G_k.

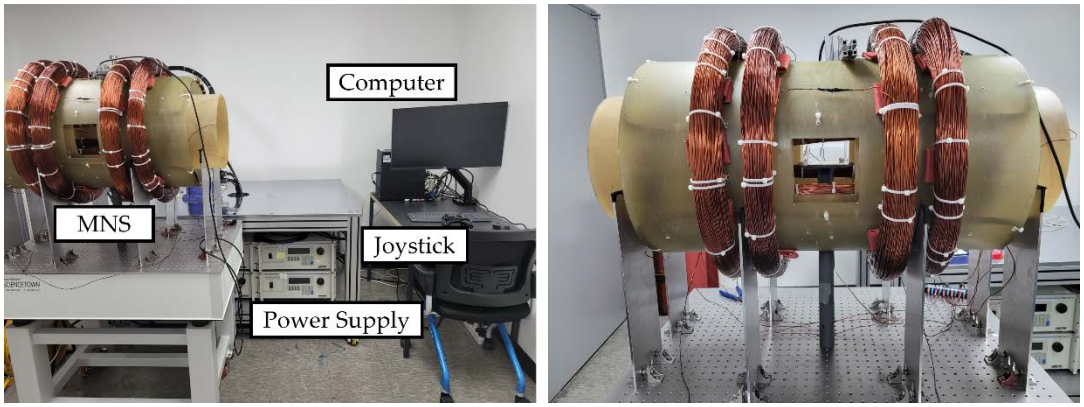

Figure 6. The constructed MNS and experimental setup to actuate a magnetic robot.

Table 2. Measured major values of the MNS.

Variables	HC	USCy	USCz1	USCz2	MC	GSC
Radius of the coil (r_k) [mm]	249.5	172.9	220.0	137.1	247.9	172.9
Resistance of the coil (R_k) [Ω]	10.2	9.8	9.0		10.1	9.0
Inductance of the coil (L_k) [mH]	405.1	364.6	170.2		303.0	248.5
Max magnetic field ($B_{k,max}$) [mT] or field gradient ($G_{k,max}$) [mT/m]	20.00	23.11	25.02		70.04	106.67

Table 3. Correction coefficients of the MNS.

	HC	USCy	USCz	MC	GSC
Correction coefficients	0.9045	0.9540	1.0313	0.8623	1.0739

3.1.2 Heating effect

The electrical insulation system for wires is divided into different classes by temperature, and we used the wire of F class for each coil. This wire has an allowable temperature of 155 degrees, and it must be a temperature limit for safe use. The temperature rises due to the current of the coils were measured by infrared thermometer as shown in Figure 7 while the maximum output power was utilized. To obtain average value, the temperatures were measured at 6 points of each coil. In the figure, the USCz1 has unlimited operating time because it converged at 96 degrees while the other coils were heated over 155 degrees. However, the USCz has limited operating time because the USCz1 and USCz2 were connected in series. Thus, all the coils of the MNS have limited operating times.

Considering the mimum operating time limit of the USCz2, the extreme operating time limit of the MNS would be 16 min. However, when we actuate a magnetic robot, each coil would be discontinuously operated below the maximum output power. Thus, the practical operating time limit of the MNS would be longer than 16 min. For example, if we generates 2D rotating magnetic field of 20 mT in xy-plane, the operating time limit would be quite larger than 40 min.

Preprints (www.preprints.org) | NOT PEER-REVIEWED | Posted: 1 July 2022 doi:10.20944/preprints202207.0011.v1

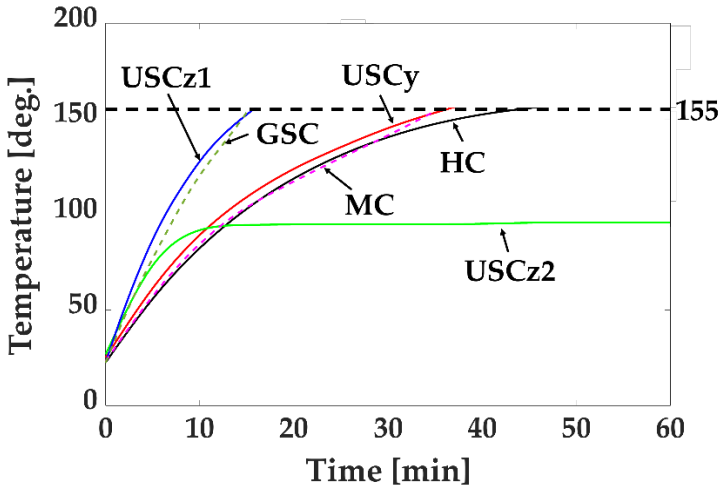

Figure 7. Temperature of coils depending on elapsed time.

3.1.3 Inductance effect

To minimize the inductance effect, each coil was designed to have a minimum inductacne within the maximum output range of the power supply unit. The current drop due to the inductance effect can be expressed as *[21]*

$$I_k = \frac{V_k}{\sqrt{R_k{}^2 + (2\pi L_k f_k)^2}} \tag{18}$$

where V_k and f_k are the input voltage and frequency of the power supply unit for kth coil. Since the magnetic field is proportional to the current in Equation (3), the calculated maximum magnetic field and filed gradient in Table 1 could not be obtained with this current drop. Figure 8 shows the measured maximum magnetic field with a variation of frequency. If we utilizes 3D rotating magnetic field, the maximum magnetic field considering the frequency of the HC should be considered because it limits the amplitude of 3D rotating magnetic field. In particular, it was observed that the amplitude of each maximum magnetic field dropped to 50 % or less at 20 Hz.

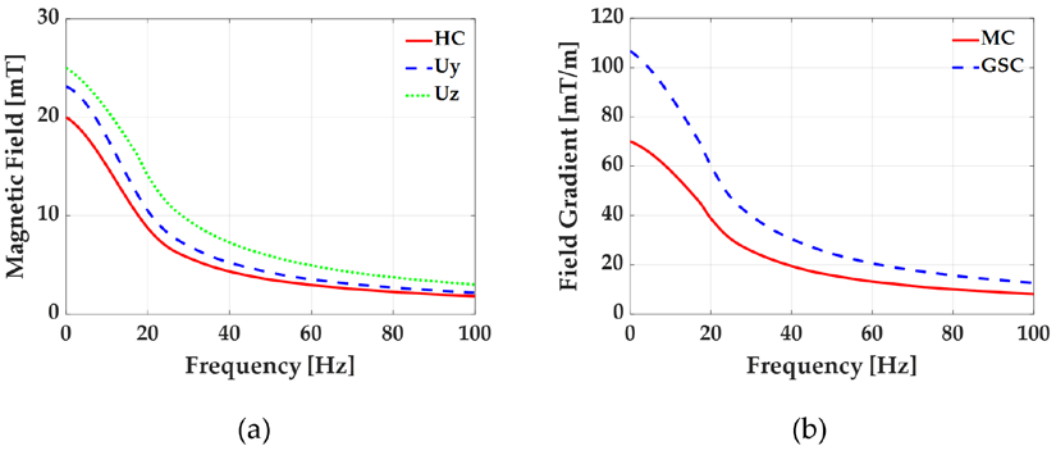

Figure 8. Calculated and measured maximum magnetic field of each coil with a variation of frequency.

3.2. Performance improvement of the optimized MNS

Preprints (www.preprints.org) | NOT PEER-REVIEWED | Posted: 1 July 2022 doi:10.20944/preprints202207.0011.v1

3.2.1 Comparison to the conventional system

To verify the optimized MNS, we compared the optimized MNS with the conventional MNS in the references *[21,22]* as shown in Tables 4 and 5. We selected this conventional MNS because it has the same maximum output power and similar outer and inner diameter of the optimized MNS. As shown in the Tables, the each coil of the optimized MNS can generate greater magnetic field. Especially, the maximum 3D rotating magnetic field is incrased to 42 %. In contrast, the magnetic field gradient of the MC is decreased althoug the magnetic field gradient of GSC is decreased. It is because the conventional MC was designed to have a relatively large number of turns. Thus, we observed that the MC of the conventional MNS has the doubled inductance than that of the optimized MNS in Table 4. Although several inductances of the optimized MNS become larger, the maximum inductance is reduced by 53 %, and it allows the optimized MNS generate a larger time-varying magnetic field and field gradient. We also obseved the increased operating time limit due to the enlarged crossectional area of each coil. If we consdier the extreme condition that the five coils are simultaeously utilized with the maximum output power, the optimized MNS can be operated for 7 times longer than the conventional MNS.

Table 4. Comparison of major values between the optimized the MNS and conventional MNS.

Variables		Conventional MNS	Optimized MNS	Differences [%]
Max magnetic field ($B_{k,max}$) [mT]	HC	14.18	20.00	41
	USCy	21.69	23.11	7
	USCz	14.04	25.02	78
Max magnetic field gradient ($G_{k,max}$) [mT/m]	MC	121.3	70.04	-42
	GSC	83.70	106.67	27
Inductance (L_k) [mH]	HC	344.5	405.1	18
	USCy	201.3	364.1	81
	USCz	394.3	170.2	-57
	MC	859.9	303.0	-65
	GSC	84.60	248.5	194
Operating time limit with Max power [min]	HC	7	60	757
	USCy	15	40	167
	USCz	10	16	60
	MC	14	35	150
	GSC	2	17	750
Diameter of an MNS [mm]	Outer	470	526	12
	Inner	235	240	2
Max power for each coil [W]		2100	2100	-

Table 5. Comparison of practical values between the optimized the MNS and conventional MNS.

Variables	Conventional MNS	Optimized MNS	Differences [%]
Max 3D rotating magnetic field [mT]	14.04	20.00	42
Min magnetic field gradient [mT/m]	83.70	70.04	-16
Max inductance [mH]	859.9	405.1	-53
Min operating time limit of the coils with Max power [min]	2	16	700

3.2.2 Performance test using a rotating magnetic field

Preprints (www.preprints.org) | NOT PEER-REVIEWED | Posted: 1 July 2022 doi:10.20944/preprints202207.0011.v1

The maximum 3D rotating magnetic field of the optimized MNS is 42 % larger than that of the conventional MNS in a static state. In addition, the porposed MNS can generate stronger time-varying magnetic field with the smaller inductance effect because the inductance was improved by 53 %. To verify how much this improvements affect on the performance of a robot, we compared the unclogging ability of a helical robot in each MNS as shown in Figure 9. First, the step-out frequencies of the helical robot were measured by the maximum 3D rotating magnetic fields of the two MNSs. The measured step-out frequency of the optimized MNS was 18 Hz which is 38 % improved value than the conventional step-out frequency of 13 Hz. Theses frequency difference may affect the drilling ability of a robot. As shown in Figure 9(b), the helical robot was actuated in front of the clogged area by agar. Considering the frictional energy consumtion during the unclogging motion, a slightly lower frequencies (17 Hz and 12 Hz) than the step-out frequencies (18 Hz and 13 Hz) were utilized for each experiment. As a result, the unclogging time was improved by 54 % from 96 sec to 44 sec. Although the performance improvement may vary depending on the type and size of a robot, this experiment shows that the performance of a magnetic robot can be effectively improved using the optimized MNS.

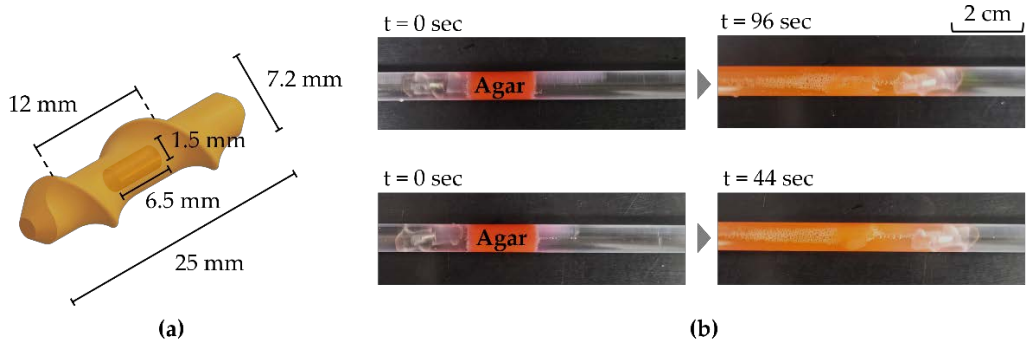

Figure 9. (a) Helical robot made of a diametrically magnetized cylindrical magnet (N52 grade) for the demonstration. (b) Unclogging motion of the helical robot inside the optimized and conventional MNS. The optimized MNS and conventional MNS generate the 3D rotating magnetic field at 17 Hz and 12 Hz, respectively.

4. Conclusions

In this paper, we proposed a methodology to optimize the MNS with the saddle coils. The MNS was optimized to generate greater magnetic field and field gradient than that of the conventional MNS which has the same output power and similar size. We also considered the heat and inductance effect of the coils so that the MNS could generate stronger time-varying magnetic field with the 7 times longer operating time limit. As a result, each coil could generate and average 22 % stronger magnetic field or field gradient while the maximum 3D rotating magnetic field was improved by 42 %. Finally, we demonstrated the unclogging performance of a helical robot was improved by 54 %, and this improvement would be achieved with most magnetic robots.

The proposed optimization methodology increases the cross-sectional area of the coils to suppress the temperature rise of the coils by reducing the current density. However, this may cause a rise in material cost because the coil made of copper is quite expensive. Thus, too large cross-sectional area of the coil is not recommended in terms of cost. Although the thickness of the wire was limited, it was still thick to manufacture the complex coils without manufacturing errors, so thickness of wire should be carefully determined considering shapes and volumes of the coils.

Author Contributions: Project administration and Funding acquisition, J.N.; Investigation, S.K. and M.C.; Methodology, S.K. and J.N.; Validation, S.K., M.C., S.I., J.Y., and J.N.; Visualization, S.K.;

Writing-original draft, S.K.; Writing—review & editing, S.K. and J.N. All authors have read and agreed to the published version of the manuscript.

Funding: This work was supported by the National Research Foundation of Korea (NRF) grant funded by the Korean government (MSIT) (No. 2021R1C1C1014661.) and the Research Grant of Kwangwoon University in 2020.

Institutional Review Board Statement: Not applicable.

Informed Consent Statement: Not applicable.

Data Availability Statement: Not applicable.

Conflicts of Interest: The authors declare no conflict of interest.

References

1. Nam, J.; Lai, Y.P.; Gauthier, L.; Jang, G.; Diller, E. Resonance-Based Design of Wireless Magnetic Capsule for Effective Sampling of Microbiome in Gastrointestinal Tract. *Sensors and Actuators A: Physical* **2022**, *342*, 113654, doi:10.1016/j.sna.2022.113654.
2. Shokrollahi, P.; Lai, Y.P.; Rash-Ahmadi, S.; Stewart, V.; Mohammadigheisar, M.; Huber, L.-A.; Matsuura, N.; Zavodni, A.E.H.; Parkinson, J.; Diller, E. Blindly Controlled Magnetically Actuated Capsule for Noninvasive Sampling of the Gastrointestinal Microbiome. *IEEE/ASME Transactions on Mechatronics* **2021**, *26*, 2616–2628, doi:10.1109/TMECH.2020.3043454.
3. Forbrigger, C.; Lim, A.; Onaizah, O.; Salmanipour, S.; Looi, T.; Drake, J.; Diller, E.D. Cable-Less, Magnetically Driven Forceps for Minimally Invasive Surgery. *IEEE Robotics and Automation Letters* **2019**, *4*, 1202–1207, doi:10.1109/LRA.2019.2894504.
4. Bernat, J.; Gajewski, P.; Kapela, R.; Marcinkowska, A.; Superczyńska, P. Design, Fabrication and Analysis of Magnetorheological Soft Gripper. *Sensors* **2022**, *22*, 2757, doi:10.3390/s22072757.
5. Lee, W.; Nam, J.; Kim, J.; Jung, E.; Kim, N.; Jang, G. Steering, Tunneling, and Stent Delivery of a Multifunctional Magnetic Catheter Robot to Treat Occlusive Vascular Disease. *IEEE Transactions on Industrial Electronics* **2020**, 1–1, doi:10.1109/TIE.2020.2965480.
6. Kim, M.-C.; Kim, E.-S.; Park, J.-O.; Choi, E.; Kim, C.-S. Robotic Localization Based on Planar Cable Robot and Hall Sensor Array Applied to Magnetic Capsule Endoscope. *Sensors* **2020**, *20*, 5728, doi:10.3390/s20205728.
7. Ji, D.-M.; Jung, W.-S.; Kim, S.-H. Wireless Manipulation Mechanism and Analysis for Actively Assistive Pinch Movements. *Sensors* **2021**, *21*, 6216, doi:10.3390/s21186216.
8. Mahoney, A.W.; Sarrazin, J.C.; Bamberg, E.; Abbott, J.J. Velocity Control with Gravity Compensation for Magnetic Helical Microswimmers. *Advanced Robotics* **2011**, *25*, 1007–1028.
9. Jeong, S.; Choi, H.; Cha, K.; Li, J.; Park, J.; Park, S. Enhanced Locomotive and Drilling Microrobot Using Precessional and Gradient Magnetic Field. *Sensors and Actuators A: Physical* **2011**, *171*, 429–435, doi:10.1016/j.sna.2011.08.020.
10. Bell, D.J.; Leutenegger, S.; Hammar, K.M.; Dong, L.X.; Nelson, B.J. Flagella-like Propulsion for Microrobots Using a Nanocoil and a Rotating Rlectromagnetic Field. In Proceedings of the 2007 IEEE International Conference on Robotics and Automation; April 2007; pp. 1128–1133.
11. Choi, H.; Cha, K.; Jeong, S.; Park, J.-O.; Park, S. 3-D Locomotive and Drilling Microrobot Using Novel Stationary EMA System. *IEEE/ASME Transactions on Mechatronics* **2013**, *18*, 1221–1225, doi:10.1109/TMECH.2012.2201494.
12. Choi, H.; Choi, J.; Jeong, S.; Yu, C.; Park, J.; Park, S. Two-Dimensional Locomotion of a Microrobot with a Novel Stationary Electromagnetic Actuation System. *Smart Mater. Struct.* **2009**, *18*, 115017, doi:10.1088/0964-1726/18/11/115017.
13. Arcese, L.; Fruchard, M.; Ferreira, A. Adaptive Controller and Observer for a Magnetic Microrobot. *IEEE Transactions on Robotics* **2013**, *29*, 1060–1067, doi:10.1109/TRO.2013.2257581.
14. Yesin, K.B.; Vollmers, K.; Nelson, B.J. Modeling and Control of Untethered Biomicrorobots in a Fluidic Environment Using Electromagnetic Fields. *The International Journal of Robotics Research* **2006**, *25*, 527–536, doi:10.1177/0278364906065389.

15. Yu, C.; Kim, J.; Choi, H.; Choi, J.; Jeong, S.; Cha, K.; Park, J.; Park, S. Novel Electromagnetic Actuation System for Three-Dimensional Locomotion and Drilling of Intravascular Microrobot. *Sensors and Actuators A: Physical* **2010**, *161*, 297–304, doi:10.1016/j.sna.2010.04.037.
16. Jeon, S.; Jang, G.; Choi, H.; Park, S. Magnetic Navigation System with Gradient and Uniform Saddle Coils for the Wireless Manipulation of Micro-Robots in Human Blood Vessels. *IEEE Transactions on Magnetics* **2010**, *46*, 1943–1946, doi:10.1109/TMAG.2010.2040144.
17. Jeon, S.M.; Jang, G.H.; Choi, H.C.; Park, S.H.; Park, J.O. Magnetic Navigation System for the Precise Helical and Translational Motions of a Microrobot in Human Blood Vessels. *Journal of Applied Physics* **2012**, *111*, 07E702, doi:10.1063/1.3671411.
18. Jeon, S.M.; Jang, G.H.; Choi, H.C.; Park, S.H.; Park, J.O. Utilization of Magnetic Gradients in a Magnetic Navigation System for the Translational Motion of a Micro-Robot in Human Blood Vessels. *IEEE Transactions on Magnetics* **2011**, *47*, 2403–2406, doi:10.1109/TMAG.2011.2148168.
19. Choi, H.; Cha, K.; Choi, J.; Jeong, S.; Jeon, S.; Jang, G.; Park, J.; Park, S. EMA System with Gradient and Uniform Saddle Coils for 3D Locomotion of Microrobot. *Sensors and Actuators A: Physical* **2010**, *163*, 410–417, doi:10.1016/j.sna.2010.08.014.
20. Go, G.; Choi, H.; Jeong, S.; Lee, C.; Ko, S.Y.; Park, J.-O.; Park, S. Electromagnetic Navigation System Using Simple Coil Structure (4 Coils) for 3-D Locomotive Microrobot. *IEEE Transactions on Magnetics* **2015**, *51*, 1–7, doi:10.1109/TMAG.2014.2364543.
21. Nam, J.; Lee, W.; Jang, B.; Jang, G. Magnetic Navigation System Utilizing Resonant Effect to Enhance Magnetic Field Applied to Magnetic Robots. *IEEE Transactions on Industrial Electronics* **2017**, *64*, 4701–4709, doi:10.1109/TIE.2017.2669886.
22. Nam, J.K.; Jeon, S.M.; Lee, W.S.; Jang, G.H. Control of a Three-Dimensional Magnetic Force Generated from a Magnetic Navigation System to Precisely Manipulate the Locomotion of a Magnetic Microrobot. *Journal of Applied Physics* **2015**, *117*, 17A726, doi:10.1063/1.4916033.